

# Inferring Fundamental Properties of the Flare Current Sheet Using Flare Ribbons: Oscillations in the Reconnection Flux Rates.

MARCEL F. CORCHADO ALBELO <sup>1</sup> AND MARIA KAZACHENKO <sup>1,2</sup>

<sup>1</sup>*Department of Astrophysics and Planetary Sciences, University of Colorado Boulder, 2000 Colorado Avenue, Boulder, CO 80305, USA*

<sup>2</sup>*National Solar Observatory, 3665 Discovery Drive, Boulder, CO 80303, USA*

## ABSTRACT

Magnetic reconnection is understood to be the main physical process that allows magnetic energy to be transformed into heat, motion, and particle acceleration in solar eruptions. Yet, observational constraints on properties of the reconnection region, and the dynamics that occur there are limited because of the high cadence and spatial resolution needed to capture these during a flare. By studying the evolution and morphology of post-reconnected field-lines footpoints, or flare ribbons, in the 1600 Å Atmospheric Imaging Assembly (AIA) and the Helioseismic Magnetic Imager (HMI) vector photospheric magnetic field, we estimate the magnetic reconnection flux and its rate of change with time to study the energy budget of the reconnection process and dynamics of the current sheet above. We compare high resolution data from the Slit-Jaw Imager (SJI) onboard the Interface Region Imaging Spectrograph (IRIS) with AIA observations to study the evolution of fine-structures in the flare ribbon as they spread away from the polarity inversion line. Using data from 2 M- and X-class flares, we explore the relationship between the ribbon-front fine-structure and the temporal development of bursts in the reconnection region. We quantify this burstiness by quantifying quasi-periodic pulsations (QPP's) signatures in derived reconnection rates. Additionally, we use the RibbonDB database to perform statistical analysis of 73 C- to X-class flares and identify QPP's properties using the Automated Flare Inference of Oscillations (AFINO) method. We find that the oscillations' periods range from one to eleven minutes. We discuss the physical implication of our finding and discuss future observational studies that could help us further constrain the current sheet dynamics.

*Keywords:* Magnetic Reconnection, Solar Flares, Quasi Periodic Pulsations, Current Sheet Dynamics

## 1. INTRODUCTION

Solar flares are intense localized emission of light in the solar atmosphere that cover the full electromagnetic spectrum (e.g. radio to  $\gamma$ -rays; see review by [Benz \(2017\)](#)). Larger flare are usually accompanied by coronal mass ejection (CME) which are referred to eruptive flares, while some have no CME associated with them (confined flares). Flares are understood to be associated with the release of free magnetic energy stored in the twisted and sheared coronal magnetic fields via magnetic reconnection (see reviews by [Priest & Forbes \(2002\)](#); [Hudson \(2011\)](#); [Shibata & Magara \(2011\)](#)). Although there is no direct measurement of the coronal reconnection, through the years observation and models have helped develop tools and frameworks to gain understanding of this process.

The standard model for eruptive two-ribbon flares, otherwise known as the CSHKP ([Carmichael 1964](#); [Sturrock 1966](#); [Hirayama 1974](#); [Kopp & Pneuman 1976](#)) is one such framework supported by many observations. It describes a sequence of coronal loops formed by reconnection as the magnetic reconnection point (so called X-point in 2D) moves upwards with an erupting flux rope (EFR; O-point in 2D) that is a CME. These loops are anchored in opposite magnetic polarities, and the line separating these is referred to as the polarity inversion line (PIL). Non-thermal particles accelerated directly or indirectly during the reconnection process precipitate down the newly formed flare loops and arrive at the chromosphere where density is high enough for bremsstrahlung to produce electromagnetic

radiation at various wavelengths (e.g.  $H_\alpha$ , ultraviolet, hard x-rays,  $\gamma$ -rays; (Brown 1971)). As the new flaring loops move higher into the corona the location of the energy deposition moves away from the PIL. As the chromosphere is locally heated by condensed non-thermal particles, thermal conduction forces chromospheric material to rise (so called chromospheric evaporation) and fill the reconnected flare loops, generating emission in soft x-rays (SXR) within the flare loops.

Flare ribbons are localized enhancements of emission in the upper chromosphere (some 2000 km above the solar surface) usually observed in  $H_\alpha$  and 1600 Å ultraviolet (UV) emission. Interpreted as the consequence of non-thermal particles precipitating from a coronal source, due to magnetic reconnection, into the dense chromosphere. They are the footpoints of newly reconnected flare loops.

Recent high-resolution observations of swirls and wave-breaks in flare ribbons and the structure in the ribbon front (newly brightened kernels in the chromosphere) suggest flare ribbons are connected to wave generating processes at the flare loop tops (Brannon et al. 2015) and to the existence of plasmoid structures within the current sheet (Wyper & Pontin 2021; Naus et al. 2022). Therefore the study of flare ribbons and comparison with more realistic 3D flare models will provide future insights into the physics of the current sheet and reconnection.

The CSHKP model in its traditional development represents a 2D flare scenario. Recently, there have been many attempts to create a 3D framework or extension of the CSHKP like 3D model. Pontin & Priest (2022) summarize the 3D scenario as follows: As with the original CSHKP model the coronal loops are formed by magnetic reconnection rising in height following the eruption of a CME, and the precipitation of non-thermal (accelerated directly or indirectly through reconnection) particles into the chromosphere. Reconnection is often impulsive and bursty in time and fragmented in space. Since reconnection is initially localized within one point it created two flare kernels of chromospheric emission; then during the flare rise phase reconnection spreads along current sheet above the PIL energizing the coronal arcade and forms the flare ribbons; the during the flare main phase, the ribbons move apart from the PIL. Most of the twist in the EFR is created during 3D reconnection, due to the conversion of magnetic shear at the PIL to twist in the EFR. Reconnection may occur in 3D null points which tend to form circular ribbon or through separators (surfaces that divide the volume into regions of distinct field-line connectivity), which create ribbons that are almost straight or S-shape. Flare ribbons can posses hooks-like structures at their ends, which represent the ends of flux ropes bounded by a separator. Although, this presents a much more complicated scenario it presents work in progress to understand the complicated physics involved in flares, and the extended use of flare ribbon observations.

Forbes & Lin (2000) described the quantitative relationship between the reconnected flux rate and the motion of the flare ribbons within the CSHKP model. They used the rate of photospheric magnetic flux change ( $\dot{\Phi}$ ) swept by the flare ribbon to determine the rate at which the magnetic field changes in the current sheet in 3D:

$$\frac{\partial \Phi_c}{\partial t} = \frac{\partial}{\partial t} \int B_c dS_c = \frac{\partial}{\partial t} \int B_n dS_{ribbon} = \frac{\partial \Phi_{phot}}{\partial t}. \quad (1)$$

Here the coronal magnetic field ( $B_c$ ) reconnection rate  $\frac{\partial \Phi_c}{\partial t}$  is defined by the integration of an inflow coronal magnetic field over the reconnection area. The problem is that this quantity is not readily available from observations due to difficulties in measuring the coronal magnetic field and the resolution needed to resolve the reconnection site area. However by conservation of flux we can use the change per unit time of flare ribbon magnetic flux  $\frac{\partial \Phi_{phot}}{\partial t}$  (later we referred to  $\Phi_{phot} = \int B_n dS_{rbn}$  as  $\Phi$ , where  $B_n$  is the normal component of the photospheric magnetic field, and  $dS_{rbn}$  is the area swept by the flare ribbon) to infer the change of the coronal field during magnetic reconnection. Measurements of the flare ribbon magnetic flux are relatively straightforward with our current observation capabilities. This allows the creation of databases like the RibbonDB database (Kazachenko et al. 2017) which contains reconnection fluxes and other adjacent properties for more than 3000 flares.

The simplest magnetic reconnection mechanism to explain the speed at which anti-parallel magnetic field lines enter the reconnection site and have their magnetic topologies changed is the Sweet-Parker (SP) mechanism (Sweet 1958a,b; Parker 1957, 1963). This mechanism treats a single laminar layer current sheet stretching along the full interface between the opposing magnetic fields, surrounded by plasma in ideal magnetohydrodynamic (MHD) conditions, where reconnection happens. This lead to the reconnection rate being very slow for coronal conditions,  $10^{-4}$ - $10^{-6}$  of the Alfvén speed; which is was too slow to account for a solar flare which happens at the order of tenths or hundredths of the Alfvén speed (fast reconnection). The first mechanism to explain fast reconnection is the Petschek (Petschek 1964) mechanism. This mechanism assumes a much smaller reconnection site surrounded by 4 slow MHD shocks which curve the magnetic field; the smaller reconnection makes the reconnection rate larger. Another mechanism that

could explain fast reconnection is to include Hall MHD, in which the current sheet is required to have a width of the ion inertial length for the hall current term in Ohm's law has to be taken into account. Lastly, impulsive or bursty reconnection when the current sheet undergoes a tearing instability. For a much more extensive review refer to Pontin & Priest (2022).

One of the most accepted theories of flare reconnection is the tearing mode (TM) instability. Such an instability has become popular because of its ability to explain fast reconnection within the context of (SP) reconnection or other stable current sheets. The TM has been shown to be excited when diffusion couples with magnetic forces (Furth et al. 1963), which forms enclosed magnetic flux surfaces within the current sheet during reconnection, so called magnetic islands in the context of 2D reconnection and plasmoids or flux ropes in 3D. TM can give rise to a nonlinear excitation, the plasmoid instability (PI) which allows bursty reconnection or plasmoid driven reconnection when the length to width ratio of a SP current sheet exceeds 100 (Loureiro et al. 2007; Shibata & Tanuma 2001). The nonlinear relationship arises through the lifetime of the plasmoid within the current sheet, they grow to widths larger than the current sheet, and decreases the reconnection rate. As the plasmoid is ejected it allows for inflow of more magnetic fields into the current sheet, and therefore the reconnection rate rises. As reconnection happens more plasmoids form within the current sheet facilitating intermittent reconnection. Furthermore, this process is complicated by the fact that plasmoids can interact with one another and merge, giving rise to plasmoids of different sizes (Shibata & Tanuma 2001; Uzdensky et al. 2010; Lynch et al. 2016). Particle in cell (PIC) models have shown that contracting magnetic islands can also accelerate particles trapped within them (Drake et al. 2006; Guidoni et al. 2016). Recent theoretical work has shown that non-thermal particle populations traveling through consecutive magnetic islands can give rise to a population of particles capable of producing the typical SXR and hard x-ray (HXR) emission observed during flares (Guidoni et al. 2022). They also provide a possible mechanism to explain particle acceleration contained within confined temporal enhancements or bursts.

Observations of flare light curves in multiple spectra have shown oscillatory contribution usually referred to as Quasi Periodic Pulsation (QPPs; see reviews by Nakariakov & Melnikov 2009; Van Doorsselaere et al. 2016). Their existence within the whole spectrum of flare emission suggest that different mechanisms might be taking place to give rise to oscillatory and bursty particle acceleration (see review by McLaughlin et al. 2018). Possible mechanism include MHD waves (Thurgood et al. 2017), plasmoid interactions with the flaring loops and among themselves (Kliem et al. 2000; Bárta et al. 2008; Jelínek et al. 2017), existence of termination shocks due to the superposition of reconnection outflow jets (Takahashi et al. 2017).

Our intentions are twofold. First, we provide observational reference relating reconnection rates and particle acceleration proxies. Second, we aim to understand the details of the flare reconnection process and its relationship with particle acceleration. In this paper, we study 73 events from the RibbonDB database which have co-temporal HXR and SXR observations. The structure is as follows: Section 2 describes the data we used in this study, the methods used to derive the magnetic reconnection properties from flare ribbon and magnetogram observations, and the detection algorithm to identify the QPPs. In section 3 we first shows some examples comparing spatial flare ribbon evolution to the evolution of the reconnection budget and the rate of its change with time. We then compare the reconnection flux/rate evolution with the co-temporal SXR and HXR emission and summarize the results of the 73 events. In section 4 we discuss and interpret our results in the context of recent work in the field. Finally, we summarize our finding in section 5.

## 2. DATA & METHODS

### 2.1. Data Description

In this section we describe the HMI, AIA, IRIS, Fermi, and GOES observations, and the methodology for evaluating magnetic reconnection flux and flux or rate from each instrument.

#### 2.1.1. SDO: AIA and HMI

The *Solar Dynamics Observatory* (SDO, Pesnell et al. 2012), launched in February 2010, allowed for the first time to derive high-quality spatial and temporal observations of the full-disk intensity maps in different narrow-band filters, and vector magnetic fields on the same platform. Allowing co-spatial observations of flare ribbons, and host active region photospheric magnetic fields. The *Atmospheric Image Assembly* (AIA, Lemen et al. 2012) observes in seven extreme-ultraviolet (EUV) and 3 UV channels. For the purpose of this study we use the 1600 Å intensity maps, corresponding to a characteristic temperature response of  $10^5$  K and 5000 K, sensitive to chromospheric emissions.

The spatial resolution is  $0.6''$ , and cadence is 24 seconds. The *Helioseismic Magnetic Imager* provides the photospheric magnetic field strength, inclination and azimuth (Hoeksema et al. 2014), which can be transformed into  $B_x$ ,  $B_y$ , and  $B_z$  following the description of Sun (2013); Bobra et al. (2021). To improve the quality of the signal, vector-field frames produced every 135 s were combined into a 720 second cadence observable, with a pixel resolution of  $0.5''$ .

### 2.1.2. IRIS: SJI Images

The *Interface Region Imaging Spectrograph* (IRIS, De Pontieu et al. (2014); De Pontieu et al. (2021)), launched June 27, 2013, is a NASA Small Explorer with a 20 cm telescope which observes in Far Ultraviolet (FUV) and Near Ultraviolet (NUV) passbands. The satellite has two science instruments, a Spectrograph (SG) and a Slit-Jaw Imager (SJI). The SG has a field of view (FOV) up to  $175''$ , and spatial resolution of  $0.33'' - 0.4''$  for FUV and NUV respectively. It probes a wide temperature regime from the photosphere (5000 K) to the corona ( $10^6$  K -  $10^7$  K), looking at FUV ( $1332\text{\AA} - 1358\text{\AA}$  &  $1389\text{\AA} - 1407\text{\AA}$ ), and NUV ( $2783\text{\AA} - 2835\text{\AA}$ ) lines. The SJI observes with a ranging cadence on the order of seconds with a FOV of  $175'' \times 175''$ , in four passbands probing the transition region (C II  $1335\text{\AA}$  & Si IV  $1400\text{\AA}$ ), chromosphere (Mg II k  $2796\text{\AA}$ ), and photosphere (continuum  $2830\text{\AA}$ ). To get IRIS level 2 data, which has been corrected for flat field, dark currents, systematic offsets, and geometric correction with the IDL script *iris\_prep.pro* (De Pontieu et al. 2021), we use the *extract\_irisL2data.py* Python procedure as part of the *iris.lmsalpy* Python library (<https://gitlab.com/mfcorchado/iris.lmsalpy>).

### 2.1.3. Fermi: GBM

The *Fermi* Gamma-ray Space Telescope (*Fermi*, Atwood et al. (2009)) was launched by NASA on June 11 2008, and has two instruments, the *Large Area Telescope* (LAT) and the *Gamma-ray Burst Monitor* (GBM, Meegan et al. (2009)), used to observe high energy astrophysical phenomena: high-energy  $\gamma$ -ray blazars, pulsars,  $\gamma$ -ray bursts, high-energy solar flares, and many more. The LAT, serving as the primary instrument aboard *Fermi*, is a wide field-of-view imager covering an energy range of  $\approx 20$  MeV to  $\approx 300$  GeV. The GBM expands the LAT capabilities to energy ranges below those observed by LAT into the HXR range. It is composed of 12 sodium iodide scintillators and two bismuth germanate scintillators used to detect  $\gamma$ -rays and HXRs with energies ranging from  $\approx 8$  keV to  $\approx 40$  MeV. The GBM produces three data types, out of which two are temporally binned the Continuous Time (CTIME) and Continuous Spectroscopy (CSPEC), and the Time-Tagged Events (TTE). For large solar flares TTE data is usually lost, and thus CTIME and CSPEC are the best data products used to evaluate temporal and spectral evolution during flares. We use CSPEC data downloaded using the OSPEX IDL software ([https://hesperia.gsfc.nasa.gov/fermi\\_solar/analyzing\\_fermi\\_gbm.htm](https://hesperia.gsfc.nasa.gov/fermi_solar/analyzing_fermi_gbm.htm)) which observes with varying cadence from 1.0 seconds to 32.7 seconds, and default value of 4.0 seconds, in 128 quasi-logarithmic energy bins, which can be binned into the following energy channels of interest: 0 – 15 keV, 15 – 25 keV, 25 – 50 keV, 50 – 100 keV, and 100 – 300 keV.

### 2.1.4. GOES: XRT

The Geostationary Operational Environmental Satellites (GOES, Bornmann et al. (1996); Chamberlin et al. (2009); Machol et al. (2019)) is a series of geosynchronous spacecrafts flown by the National Oceanic and Atmospheric Administration (NOAA) since 1974. Their main application has been to observe the terrestrial weather and monitor many aspects of the space environment. They have always included a solar X-ray Sensor (XRS), which from their original design measure incoming solar X-ray irradiance with a cadence of 1 s in two channels,  $0.5 - 4\text{\AA}$  and  $1 - 8\text{\AA}$ , both in the SXR regimen, and corresponding to a range of  $\approx 1.5$  to  $\approx 25$  keV.

## 2.2. Methodology

In this section we first describe the selection criteria of the 73 flares in this study. We then describe how we use AIA full disk  $1600\text{\AA}$ , and IRIS SJI  $1330\text{\AA}$  and  $1400\text{\AA}$  images to create mask of the flaring ribbon area, and calculate the reconnection flux and its rate for each flare in our sample including their uncertainties. Finally we present the AFINO methodology (Inglis et al. 2015, 2016) to describe the most significant oscillating mode/frequency for each of the different types of time series in our data.

### 2.2.1. Data Selection

We selected 73 large flares from the RibbonDB database (Kazachenko et al. 2017) of various flare classes: 10 X-class, 24 M-class, and 39 C-class flares observed from 2010 - 2016. These events were selected manually and represent a

random sub-sample from more than 3000 flare events contained in the RibbonDB database. The selection was made to ensure that the events exhibited QPPs in our magnetic reconnection rate proxies, and had co-temporal irradiance time series observations from both GOES XRS and Fermi GBM instruments. Specifically, we compared 3 time series: magnetic reconnection flux/rate proxies, SXR irradiance and its rate ( $0.5 - 4 \text{ \AA}$  and  $1 - 8 \text{ \AA}$ ), and HXR irradiance ( $0 - 15 \text{ keV}$ ,  $15 - 25 \text{ keV}$ ,  $25 - 50 \text{ keV}$ ,  $50 - 100 \text{ keV}$ , and  $100 - 300 \text{ keV}$ ).

In addition, we used IRIS SJI observations to examine fine-structure in flare ribbon fronts for eight events. The SJI observation yielded twin flare ribbon morphology evolution similar to that observed by the AIA  $1600 \text{ \AA}$ , and used to calculate the reconnection flux and rate proxies. Yet, because of their smaller FOV they failed to always capture the full area in which the flare ribbon kernels were observed by AIA, and therefore only used to observe of fine-structure development in particular regions of the ribbons for 8 of the 73 events in which IRIS was co-temporally observing the on-disk flaring cites.

### 2.2.2. SDO: Magnetic Reconnection Flux and Rates

To identify the reconnection flux  $\Phi(t)$ , we use the vertical component of the HMI vector magnetic field maps, and ribbon maps. To identify the ribbon area  $A_{rbn}(\vec{x}, t; c)$ , we use the procedure described in [Kazachenko et al. \(2017\)](#), for AIA and IRIS SJI images. Then the reconnection flux:

$$\Phi^{(I_c)}(t) = \int dA_{rbn}(\vec{x}, t; c) B_n(\vec{x}, t) \quad (2)$$

$$\Phi^{(I_c)}(t_k) \approx \sum_i^{N_i} \sum_j^{N_j} \mathcal{M}^{(I_c)}(x_i, y_j, t_k) B_r(x_i, y_j, t_k) \Delta A. \quad (3)$$

The numerical approximation of the function  $\Phi(t)$  is defines as  $\Phi(t_k)$ . In this numerical approximation  $\mathcal{M}^{(I_c)}(x_i, y_j, t_k)$  refers to the cumulative mask at a time  $t_k$  of the sequence of AIA or IRIS SJI images,  $x_i$  and  $y_j$  refer to the horizontal position of a given pixel,  $\Delta A$  refers to the pixel area size, and  $I_c$  to the cutoff intensity criteria to identify the flare ribbon pixels. The cumulative mask  $\mathcal{M}^{(I_c)}(x_i, y_j, t_k) = \mathcal{M}^{(I_c)}(x_i, y_j, t_{k-1}) \cup \mathcal{N}^{(I_c)}(x_i, y_j, t_k)$  is defined as the set of all the flaring pixels in the instantaneous mask  $\mathcal{N}^{(I_c)}(x_i, y_j, t_k) \in I \geq I_c$  up to the image “k” in the sequence of observations. For IRIS SJI images the intensity maps have to be co-aligned with the HMI field of view in order to evaluate the reconnection flux. Furthermore, since IRIS SJIs have higher spatial resolution than the HMI maps, we first cut-out the IRIS FOV from the HMI maps and up-scale them to match the dimensions of the IRIS SJI using SunPY ([Mumford et al. 2020, 2022](#)) and AstroPY ([The Astropy Collaboration et al. 2022](#)).

We make use of a cumulative flare ribbon to account for flaring pixels that might be offset by the brightness increase of the flaring region as the flare evolves from gradual to impulsive phase, and the short lifetime of some flaring pixels. Thus, once a pixel has brightened up and is larger than  $I_c$ , it is included as part of the flare ribbon mask, until the end of the event. The cutoff intensity, which determines if a bright pixel belongs to the instantaneous flare ribbon mask, is defined as  $I_c(t_k) = \text{median}(I(x_i, y_j, t_k)) \cdot c$ . We use the median as it measures the central value of the intensity maps, which we use as a proxy for the intensity of the background chromosphere emission, with a lower bias to the flaring pixels; as compared to the mean intensity. We use the cutoff parameter  $c = \{6, 8, 10\}$  from empirical results both for the  $1600 \text{ \AA}$  AIA, and  $1330$  and  $1400 \text{ \AA}$  IRIS SJI intensity maps. With this range of cutoff intensities we define the positive and negative reconnection flux and the error in these estimates, for each positive (+) and negative (−) polarity:

$$\Phi^\pm(t_k) = \frac{\Phi^{\pm I_6}(k) + \Phi^{\pm I_{10}}(t_k)}{2}. \quad (4)$$

$$\delta\Phi^\pm(t_k) = \frac{|\Phi^{\pm I_{10}}(t_k) - \Phi^{\pm I_6}(t_k)|}{2}. \quad (5)$$

The reconnection flux rate for each magnetic polarity is then defined as the time derivative of the reconnection flux  $\dot{\Phi}^\pm(t_k) = \frac{\Phi^\pm(t_{k+1}) - \Phi^\pm(t_{k-1})}{t_{k+1} - t_{k-1}}$ . The uncertainty in the reconnection rate for any given time can be estimated using the same formalism as for the reconnection flux:



$$\delta\dot{\Phi}^{\pm}(t_k) = \frac{|\dot{\Phi}^{\pm I_{10}}(t_k) - \dot{\Phi}^{\pm I_6}(t_k)|}{2}. \quad (6)$$

Finally, for more clear comparison the magnetic reconnection flux and rate proxies to the observed SXR and HXR irradiances we quantify the unsigned time series of each of the reconnection observable and ad-hoc estimations of their uncertainties. First, we define both the reconnection fluxes and rates as the average between the absolute value of the positive and negative polarity observables:

$$\Phi(t_k) = \frac{\Phi^+(t_k) + |\Phi^-(t_k)|}{2}, \quad (7)$$

$$\dot{\Phi}(t_k) = \frac{\dot{\Phi}^+(t_k) + |\dot{\Phi}^-(t_k)|}{2}. \quad (8)$$

We then define the uncertainty of these measurements as the absolute value of the difference in the observables from each polarity:

$$\delta\Phi(t_k) = \frac{|\Phi^+(t_k) - |\Phi^-(t_k)||}{2}, \quad (9)$$

$$\delta\dot{\Phi}(t_k) = \frac{|\dot{\Phi}^+(t_k) - |\dot{\Phi}^-(t_k)||}{2}. \quad (10)$$

This calculation is based on the fact that both the reconnection budget and the rates should be equal in each of the polarities since they correspond to the same flaring loop system.

### 2.2.3. SDO: Analyzing Quasi-Periodic Pulsations

Similar to other astrophysical processes the Fourier power spectrum of the magnetic reconnection rates follows a power law distribution with frequency. Thus, identifying modes of oscillation from the Fourier power spectrum can be complicated. To analyze the QPPs in the magnetic reconnection rates we follow the suggestion of [Broomhall et al. \(2019\)](#), and use the *Automated Flare Inference of Oscillations* (AFINO [Inglis et al. \(2015, 2016\)](#)). This method is notorious for its good performance compared to other methods used to automatically detect stationary QPPs in flares. One of the advantages of AFINO over other methods is that it does not require complex preparation of the data before being used as input for AFINO, including time dependant detrending of the data. Time dependant detrending of the signal can affect the distribution of its Fourier power spectrum, and lead to incorrect identification of the frequency of the oscillation modes. The AFINO methodology is explained in great detail in [Inglis et al. \(2015, 2016\)](#) and can be implemented in Python using the AFINO GITHUB repository ([https://github.com/aringlis/afino\\_release\\_version](https://github.com/aringlis/afino_release_version)); here we briefly summarize the most important steps:

1. Normalize the signal and shift the mean to zero  $S^*(t_k) = \frac{S(t_k) - \text{mean}(S)}{\text{mean}(S)}$ .
2. Calculate the Fast Fourier Transform (FFT) of the normalized signal ( $\hat{S}^*(f)$ ).
3. Define models of the Fourier Power Spectrum: Power law ( $M_0$ ), Gaussian Enhanced Power Law ( $M_1$ ), Broken Power Law ( $M_2$ ).

$$M_0(f) = A_0 f^{\alpha_0} + C_0, \quad (11)$$

$$M_1(f) = A_1 f^{\alpha_1} + B \exp\left(\frac{-(\ln f - \ln f_p)^2}{2\sigma^2}\right) + M_1, \quad (12)$$

$$M_2(f) = \begin{cases} A_2 f^{-\alpha_a} + C_2 & f < f_{break}, \\ A_2 f_{break}^{-(\alpha_a + \alpha_b)} f^{-\alpha_b} + C_2 & f > f_{break}. \end{cases} \quad (13)$$

$$(14)$$

4. Evaluate the most likely fit of each model out of 20 iterations using the maximum likelihood, where  $\hat{\mathcal{S}}^* = \{s_i, \dots, s_{N/2}\}$  represent the real part of the Fourier power spectrum of the normalized signal and  $M = \{m_i, \dots, m_{N/2}\}$  represents the modeled Fourier power spectrum (Vaughan 2005).

$$L = \prod_{j=1}^{N/2} \frac{1}{m_j} \exp\left(-\frac{s_j}{m_j}\right) \quad (15)$$

5. Evaluate the preferred fit out of each model using the Bayesian Information Criteria (BIC), where a model  $M_i$  is strongly favored over a model  $M_j$  if  $BIC_i - BIC_j < -10$  (Burnham & Anderson 2004).

$$BIC = -2 \ln L + k \ln(N/2) \quad (16)$$

6. Evaluate a reduced  $\chi_\nu^2$  for exponentially distributed data to evaluate the wellness of the preferred model fit, with  $\nu$  free parameters (Nita et al. 2014).

$$\chi_\nu^2 = \frac{1}{\nu} \sum_{j=1}^{N/2} \left(1 - \frac{s_j}{m_j}\right)^2 \quad (17)$$

### 3. RESULTS

In this section we first show a few examples of the spatiotemporal evolution of flare ribbons as observed with AIA 1600 Å and IRIS SJI 1330 Å and 1400 Å. We then compare the calculated reconnection fluxes and rates using the HMI photospheric vector magnetograms, and finally with Fermi and GOES HXR emissions. We used AFINO to calculate the QPP period for each observation. Finally, we summarize the results of the 73 flares with co-temporal SDO, Fermi GBM, and GOES XRS observations.

#### 3.1. Example Events

##### 3.1.1. Reconnection Rate Oscillations

In Figure1(a) we show the spatiotemporal evolution of the flare ribbon for the X1.6-class flare observed for one hour on 2014-09-10:17:19 UTC. The co-temporal full-disk observation obtained from SDO: AIA and HMI allowed us to track the evolution of the flare ribbons as they swept through the active region NOAA12158 (as classified by the National Oceanic and Atmospheric Agency – NOAA). We analyzed the flare ribbons based on the magnetic polarity that they swept of the given active region. The cumulative reconnection flux increases smoothly, as seen in Figure1(b). The reconnection rate, shown in Figure1(c), uncovers more details on how the reconnection budget increases, and exhibits a series of bursts that balance each other in both polarities. These bursts gradually decay as the flare reaches its end. Additionally, we find that larger peaks in the reconnection rates correspond to earlier stages of the flare (blue) when the flare ribbons sweep the largest areas with strong magnetic field regions. Finally, the reconnected flux from each burst is estimated as the difference in the flux from the onset to the decay of each burst. In this flare the distribution of reconnected fluxes from each burst ranges from  $0.2\text{-}6 \times 10^{20}$  Mx.

##### 3.1.2. IRIS SJI Flare Ribbon Observations

To understand the details of the relationship between the flare ribbon evolution and the reconnection rate signatures we show higher spatial-resolution IRIS SJI observations in the 1330 Å and 1400 Å filters. In figures 2(a) and 3(a) we show the cumulative flare ribbon mask evolution derived from the IRIS SJI observations for the same X1.6 flare shown in Figure1(a) and from an M8.6 flare observed on 2014-10-22.

First, we analyze the X1.6 flare shown in section 3.1.1. The first thing to notice in Figure2 is that the IRIS SJI observations have a smaller FOV than the cutout from the full solar disk observations of SDO. This limits the use of these observations since they rarely capture the full flare ribbon evolution. For the reason we continue using AIA 1600 Å data to calculate our reconnection flux/rate proxies. Yet, the high spatial resolution shows fine-structure details within the flare ribbon fronts. The three snapshots from the IRIS observations (Figure2(b,c,d)) show that in times when the reconnection rate reaches a local maxima the flare ribbons exhibits fine-structure details like saw-tooth/wave-breaking patterns. However, examining the evolution of the cumulative ribbon mask we find that these fine-structure details in the flare ribbon fronts are usually not the main contributors to the reconnection flux budget. Rather, it is the complex larger-scale flare ribbon motion that is responsible for the reconnection rate oscillatory bursts.

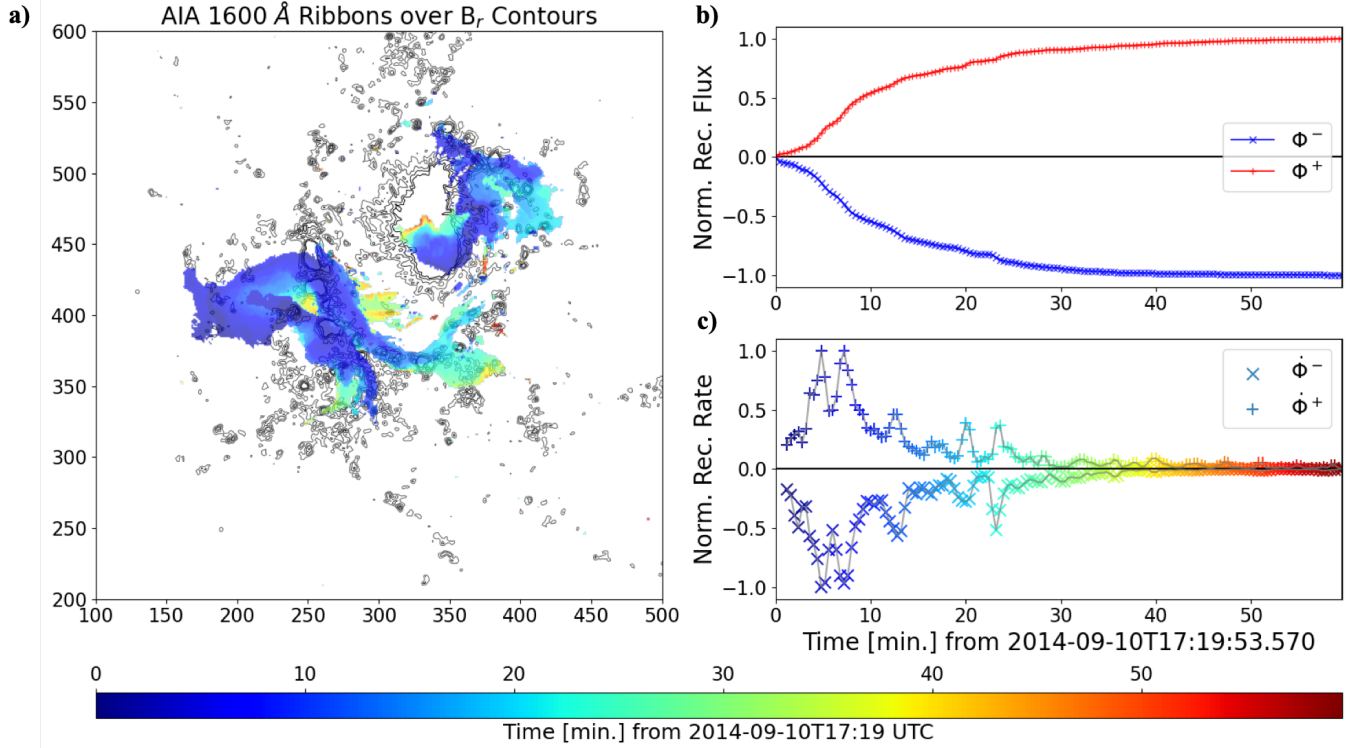


**Figure 1.** AIA 1600 Å observations of X1.6 flare on 2014-09-10: a) Evolution of cumulative flare-ribbon mask over vertical magnetic field component  $B_r$  (black contours), colored from early evolution (blue) to the end of the flare (red). b) Reconnection flux proxy within positive (red +) and negative (blue -) polarity flare ribbons. c) Reconnection rates for each of the flare ribbon corresponding to each magnetic polarity, the color corresponds to the flare ribbon cumulative mask evolution.

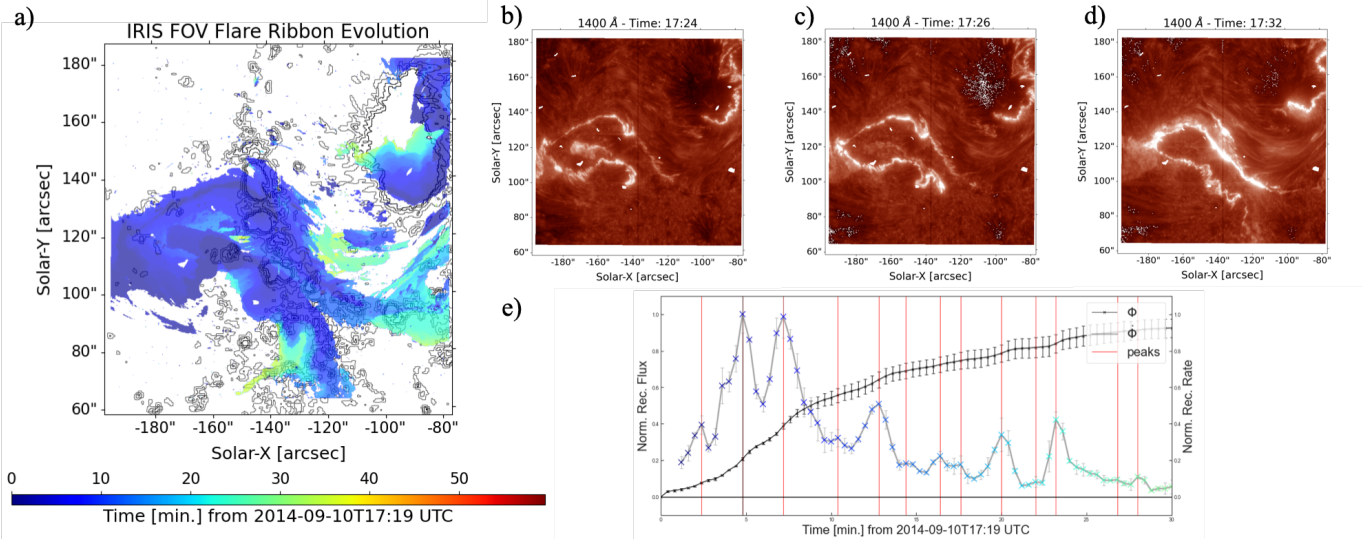


**Figure 2.** IRIS 1400 Å SJI observations of the same X-class flare as shown in Figure 1: a) IRIS 1400 Å cumulative mask evolution over HMI  $B_r$  contours with IRIS FOV. b) Flare ribbons in IRIS FOV during the reconnection rate maximum ( $t \approx 5$  minutes since start of observation). c) Same as Figure 2.b but at the second highest reconnection rate peak ( $t \approx 8$  minutes). d) Same as the previous but at a reconnection rate peak in a latter phase of the flare ( $t \approx 12$  minutes). e) Average reconnection flux (black) and rate (colored following the flare ribbon evolution) from the two magnetic polarities, the vertical red lines identify the peaks in reconnection rate using the *SciPy* library (Virtanen et al. 2020).



For the M8.6 flare on 2014-10-22, shown in Figure 3, we observe similar behavior as in Figure 2. The ribbon masks derived from IRIS observations show that during the early stages of the flare the ribbons evolution brightening are sparse through the FOV, leading to a few lower amplitude bursts visible in the reconnection rates. Approximately 20-40 minutes into the observations the ribbons grow rapidly (seen cyan to yellow colors), which match reconnection rate bursts of larger amplitudes. Later, there are still some bursts in the reconnection rate associated with continued expansion of the flare ribbons. We find that the burst contributions to the reconnection flux range from  $0.6 - 10 \times 10^{20}$  Mx. We find that there are fewer finer details in this flare compared to the X1.6 flare.

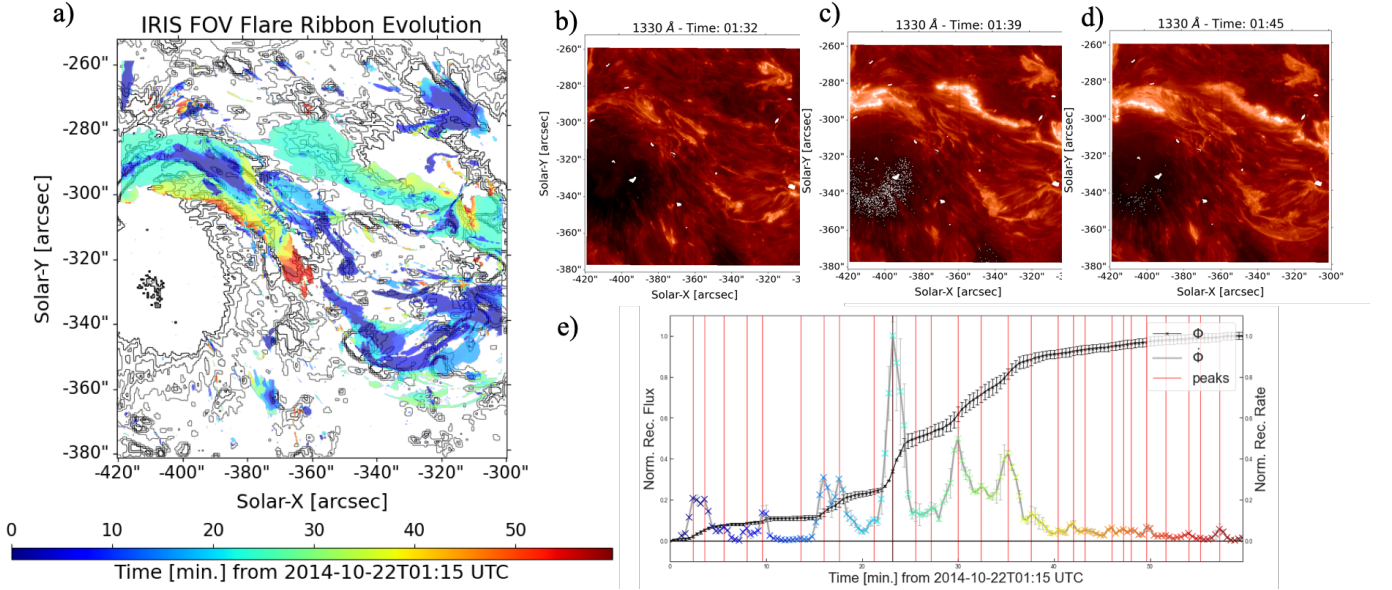


**Figure 3.** IRIS 1330 Å SJI observations of M8.6 flare on 2014-10-22: a) Cumulative flare-ribbon mask evolution. b) Flare ribbons before the reconnection rate maximum ( $t \approx 17$  minutes). c) Flare ribbons at the reconnection rate maximum ( $t \approx 24$  minutes). d) Flare ribbon after the reconnection rate maximum ( $t \approx 30$  minutes).

The fine scale structures that are observed in the high-spatial resolution IRIS SJI observations are thought to be connected to process and structures higher in the corona where magnetic reconnection with the flare loops is happening (i.e. the current sheet; Brannon et al. 2015; Wyper & Pontin 2021). In section 4 we compare this interpretation and others with our findings of magnetic-reconnection rate bursts in more detail.

### 3.1.3. Co-temporal X-ray Emission

Until now we have focused our attention on the spatial complexities of flare ribbons and their relationship with QPP burst in the magnetic reconnection rates. In this section we compare temporal evolution of the reconnection flux rate and other flare phenomena. In particular, we analyze the emission of HXR in the M8.6 flare on 2014-10-22 and M2.1 flare on 2012-03-06.

In Figure 4 we show two examples out of 73 flares included in our study of Fermi GBM, GOES XRS, and SDO observations. The left column shows the observations for the same M8.6 flare as in Figure 3. The right column compares X-ray emission and reconnection for an M2.1 flare observed on 2012-03-06. We include only those Fermi channels that are not noise-affected, and also both of the GOES channels since the SXR provides a good proxy for the HXR emission via the Neupert effect (Neupert 1968).

Both of these flares serve as an example of how the emission does not correspond 1-1 to the magnetic reconnection rate evolution. Yet, we still detect bursty emission matching the temporal profile of the reconnection rate. We notice that in spite very close temporal correspondence between the peaks of the X-ray emission and the reconnection flux rate there are some delays of approximately 20 - 40 seconds. Furthermore, lower amplitude bursts in the reconnection rates are not always accompanied by a corresponding burst in the HXR emission. This is especially noticeable when comparing early phases of the Fermi GBM with the reconnection rate profiles. For the 2014-10-22 flare the first Fermi GBM x-ray bursts are observed only 20 minutes after the flare start time.

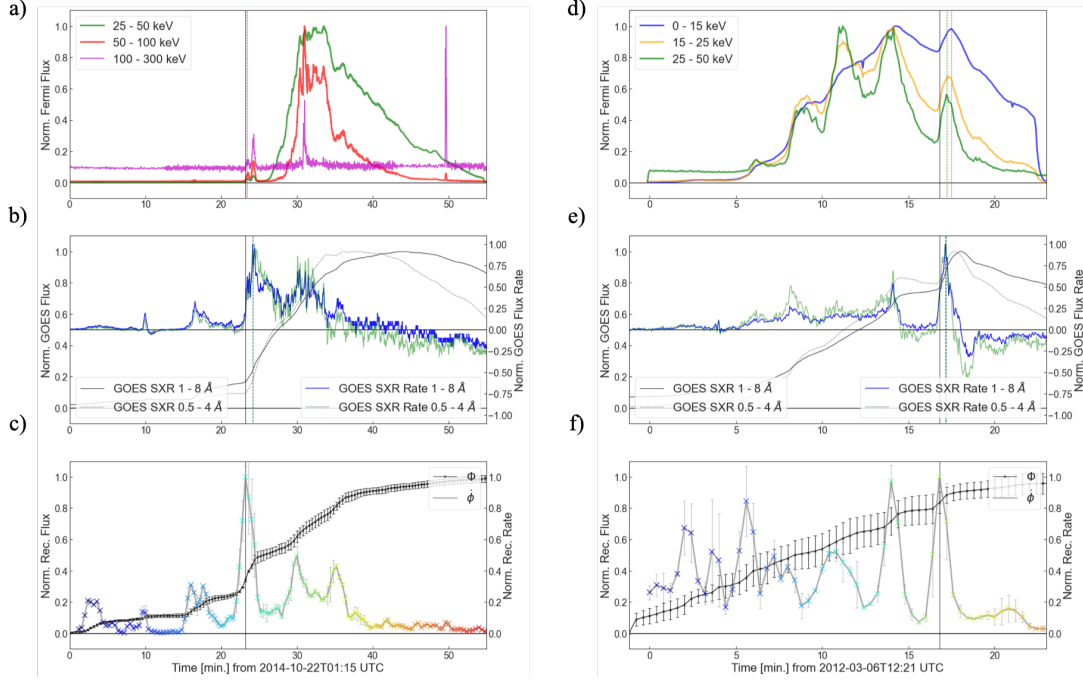


**Figure 4.** X-Ray emission observed by Fermi GBM and GOES XRS: a) Fermi GBM flux observed in 3 energy bands (25-50 keV in green, 50-100 keV in red, and 100-300 keV in magenta). b) GOES SXR flux (solid black and dotted grey) and time derivative, which is a proxy for HXR emission (blue and green) 1-8 Å and 0.5-4 Å wavelength bands respectively. c) Reconnection flux (black) and its rate (colored to scale with temporal evolution). d) Fermi GBM flux observed in 3 energy bands 0-15 keV in blue, 15-25 keV in yellow, and 25-50 keV in green. e-f) Same as b) and c) respectively. Observations presented in a-c) correspond to the M-class flare showed in Figure 3, while those from d-f) correspond to an M-class flare observed on 2012-03-06. All of the vertical lines shown in color correspond to the closest significant peak in HXR emission from the reconnection rate maximum (black).

Lastly, when applying AFINO to the reconnection rates of both of these flares, we model QPPs with periods of approximately 11 and 3 minutes correspondingly. The 11 minute QPP period oscillation found for the 2014-10-22 flare has no corresponding QPPs detected in the HXR emission. For the second flare on 2012-0-6, we find 3 minute in both the 15 - 25 keV and 25 - 50 keV channels. Thus, although the temporal signatures between channels and different instruments seem similar, the characterization and detection of QPP periods associated with them are complicated.

These co-temporal bursty signatures in both of the HXR emission observed by Fermi GBM, GOES XRS SXR emission and the reconnection rates from SDO suggest a link between the two types of observations. In section 4 we discuss this relationship in more detail.

### 3.2. Summary Results of 73 events

To understand the relationships that we found for the example events in section 3.1 we expand our analysis to 73 flares. The list consists of 39 C-class, 24 M-class, and 10 X-class flares from the RibbonDB database.

#### 3.2.1. Comparison of QPP Periods: Reconnection Rates and X-Ray Emission

We apply the AFINO methodology to the full list of flares. Figure 5 shows the distribution of periods compared with the goodness of fit measure, the reduced  $\chi^2$ . We see that most of the periods fall close to a reduced  $\chi^2 \approx 1$  which suggests that the QPP model is a good fit for most of the reconnection rate events. Although the QPP model is a good fit for most events the reduced  $\chi^2$  does distinguish if it is the only model to accurately represent the data. We use the criteria  $\Delta\text{BIC} \leq -10$  (colored in yellow, Burnham & Anderson 2004) to distinguish whether the model QPP model is statistically preferred from a pure noise model shown in equation 11. We refer to an AFINO detection for each flare event when both the conditions described above are satisfied. Figure 5 shows our result shows a large distribution of QPP periods modeled with AFINO ranging from approximately 1 to 11 minutes. We find 26 detections with a strong preference for the QPP model out of the 73 flares.

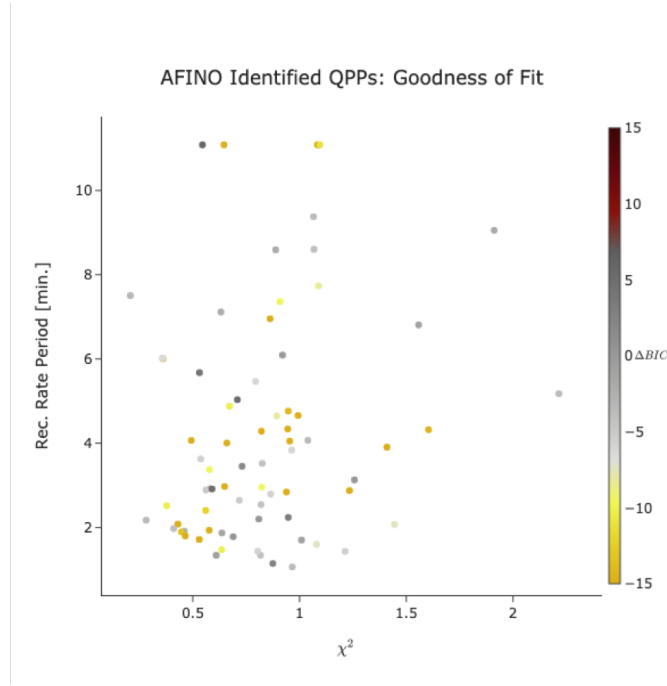


**Figure 5.** Distribution of QPP periods in unsigned reconnection-rates averages for the 73 flares. AFINO detection corresponds to QPP periods with  $\Delta \text{BIC}(\text{QPP-Noise}) \leq -10$  (yellow) and  $\chi^2 \approx 1$ .

When comparing the QPP periods modeled with AFINO in the Fermi GBM HXR emission we find that there are very few detections for each channel. Figure 6 shows that the lower energy channels (0 - 50 keV) observe emission in a large number of flares. Furthermore, at these same lower energy channels the QPP low period QPPs in the reconnection rate are more consistent with those modeled in the HXR, even if the flare do not correspond strictly to AFINO detections. Events with QPP periods in the reconnection rates above five minutes tend to have a larger scatter in their corresponding HXR QPP period.

The higher energy channels (50 - 100 keV) include a very low number of flares, found to be limited to a small sample of X- and M- class flares. Figure 6(d,e) show an even lower number of AFINO detections which is appropriate due to the smaller sample size of flare containing emission in these channels. Therefore, it is more difficult to establish any trends between the QPPs in the reconnection rate with those of the HXR emission at high energies.

The results from the GOES XRS flux derivative shown in Figure 7 are similar to those from the Fermi GBM. Since the wavelength bands of the GOES XRS are closer to each other than the energy channels in the Fermi GBM data we see a similar number of flare events in each band. As was the case with the Fermi GBM periods, detection of events for which the QPP model is preferred are low. Furthermore, the linear relationship found for flares with low periods in their reconnection rates and Fermi GBM HXR emission (below 50 keV) is not found in the GOES SXR derivative QPPs.

Our result suggests that although the QPP model can be used to characterize the bursts in the reconnection rates with AFINO, it usually fails to detect HXR QPPs that share the same periods, above 5 minutes. In most cases a detection of a QPP in the reconnection rate will not guarantee that the bursty emission of HXRs can be classified as a QPP by AFINO nor that it will share the same period. Yet, as seen by the linear relationship between the low period QPPs in the reconnection rate and Fermi HXR emission (< 50 keV) AFINO detections are very strict and biases such as low sample size and presence of oscillation modes below the AIA cadence Nyquist frequency. In section 4 we will discuss the complexity of detecting QPPs of the same period in our two types of observations.

### 3.2.2. Delay in X-Ray Emission

When examining individual examples presented in Figure 4, we found that the HXR emission from both the Fermi GBM and GOES XRS was delayed from the reconnection rate bursts. To track the delay time of the HXR emission for each of the flares we first detect the maximum in the reconnection rate, and then find the closest local maxima in the X-ray emission. The time difference between the reconnection rate maximum (set as  $t = 0$  seconds) and the closest

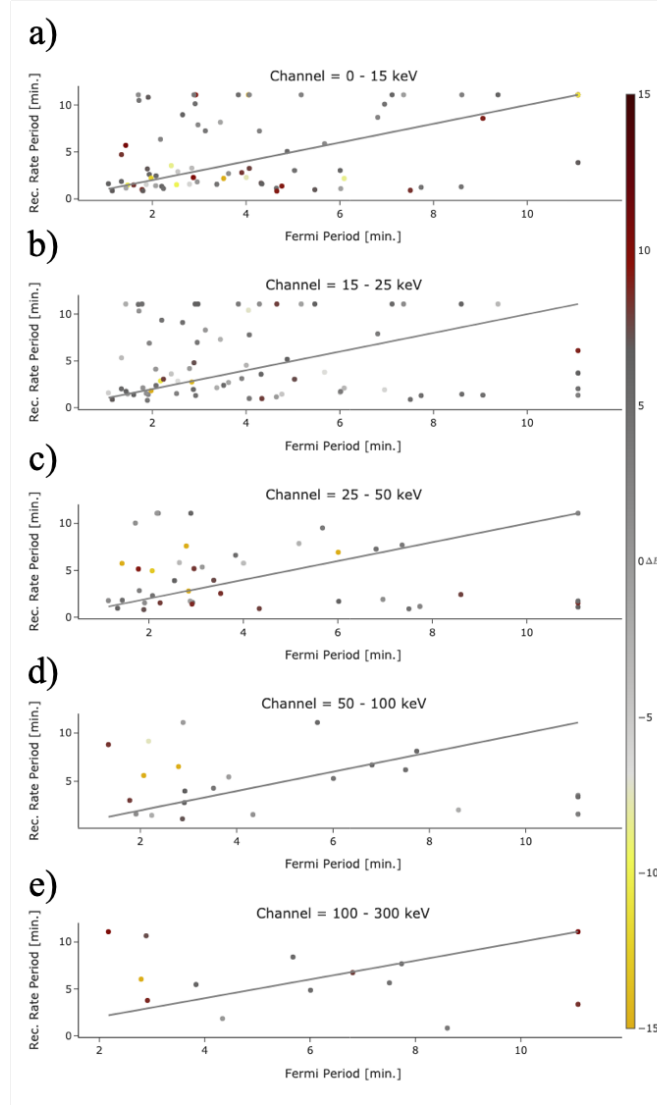


**Figure 6.** Distribution QPP periods in unsigned reconnection rate averages compared to those in each Fermi GBM channel: a) 0-15 keV, b) 15-25 keV, c) 25-50 keV, d) 50-100 keV, and e) 100-300 keV. AFINO detection is proxied with  $\Delta BIC_{Fermi} \leq -10$  (yellow).

local maxima in the x-ray emission is referred to as the delay time between the signals. The window to search for a local maxima in the HXR emission is increased up to two minutes, empirically for simplicity and avoiding detecting a larger subsequent/previous HXR emission burst.

Figure 4 shows the delay time in the Fermi GBM HXR emission has similar profiles for each of the energy channels. Each row in the left panel show distributions of delay times in HXR emission centered around 24 seconds. Only the lowest energy channel (0-15 keV) shows a bimodal distribution, with the second peak corresponding to approximately 2 minutes. This secondary peak is not present in any of the other energy channels and we attribute to a bias created by the window size of our peak detection. This is because the emission in the lower channel is more easily saturated, and as a consequence the identification of the local maxima using our simple detection algorithm fails.

The 24 second delay time corresponds to the time cadence of the AIA observations. Therefore they could be a systematic effect from the finite difference scheme used to calculate the reconnection rate. The second column of Figure 8 shows the delay times for the 25-50 keV channel derived using two different finite difference schemes to approximate the reconnection rate: forward and backwards finite differences, as opposed to the central difference scheme which is the default of the *NumPy* library (Harris et al. 2020) used to derive the reconnection rate. Changes

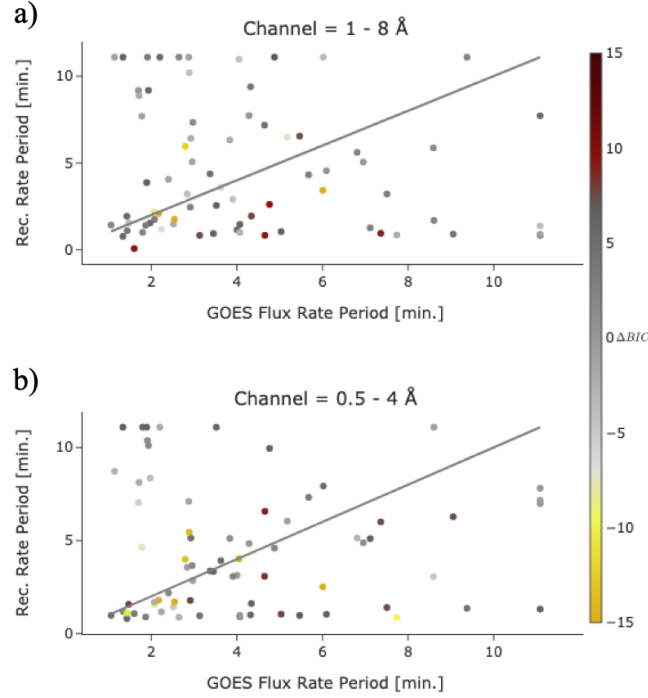


**Figure 7.** Distribution QPP periods in unsigned reconnection-rates averages compared to those in each HXR proxy derived from GOES XRS bandwidths: a) 1-8 Å, b) 0.5-4 Å. AFINO detection is proxied with  $\Delta BIC \leq -10$  (yellow).

in the numerical approximation of the derivatives causes no significant changes to the location of the mode of the distribution. Therefore, this delay in the HXR emission is not an artifact of the finite difference scheme.

The results of the GOES XRS HXR emission proxy in both channels have peaks in their delay distributions that are centered within the range of 0 - 24 seconds for the central difference derivative scheme as seen in Figure 9(a). The distribution of delay times suggest that this proxy of the HXR emission tends to be more co-temporal to the reconnection rate bursts compared to Fermi GBM observations. The center and right columns of Figure 9(c,d) show that changes in finite difference scheme used in the numerical approximation of the reconnection rate has a more significant effect in the distribution of delay times for GOES HXR emission. We explain this higher sensitivity consequence of the initial distribution being more uniform (for  $0 \leq \text{delay} \leq 120$ ) than those found for the HXR emission. Therefore, the redistribution of the delay time distribution could more easily shift the delay time peak. Yet, most of the flare displays a delay in the GOES HXR emission proxy that is the order of seconds to minutes, agreeing with the results from the Fermi HXR emissions.

#### 4. DISCUSSION

Our spatiotemporal analysis of the flare ribbons and the reconnection rate time series showed that the addition of new magnetic flux swept by the flare ribbons produces bursts in magnetic reconnection. Bursty magnetic reconnection is associated with the plasmoid instability (PI), and the formation and dynamics of plasmoids of different scales within the current sheet (Shibata & Tanuma 2001). Analytical work (Wyper & Pontin 2021) suggest that this swirls and wave breaking pattern shown in figures 2 and 3 can be related to PI. In particular, Wyper & Pontin (2021) used an analytical representation of an eruptive flux rope and flaring loop system to show that plasmoid structures within the current sheet were connected to the fine structure displayed in the flare ribbons.

Brannon et al. (2015) found QPP signatures in the position and Doppler shifts of sawtooth fine structure (wave breaks) patterns with periods of 140 seconds and 100 to 200 seconds respectively, which are within the period range of detected QPPs from the reconnection rates found here (1 - 11 minutes). We found a QPP period of 197 seconds in the reconnection rate of this event, which agrees with their findings. Brannon et al. (2015); Parker & Longcope (2017) both suggested that a possible explanation of the oscillations found in the motions of the fine-structure in the flare ribbon was the PI.



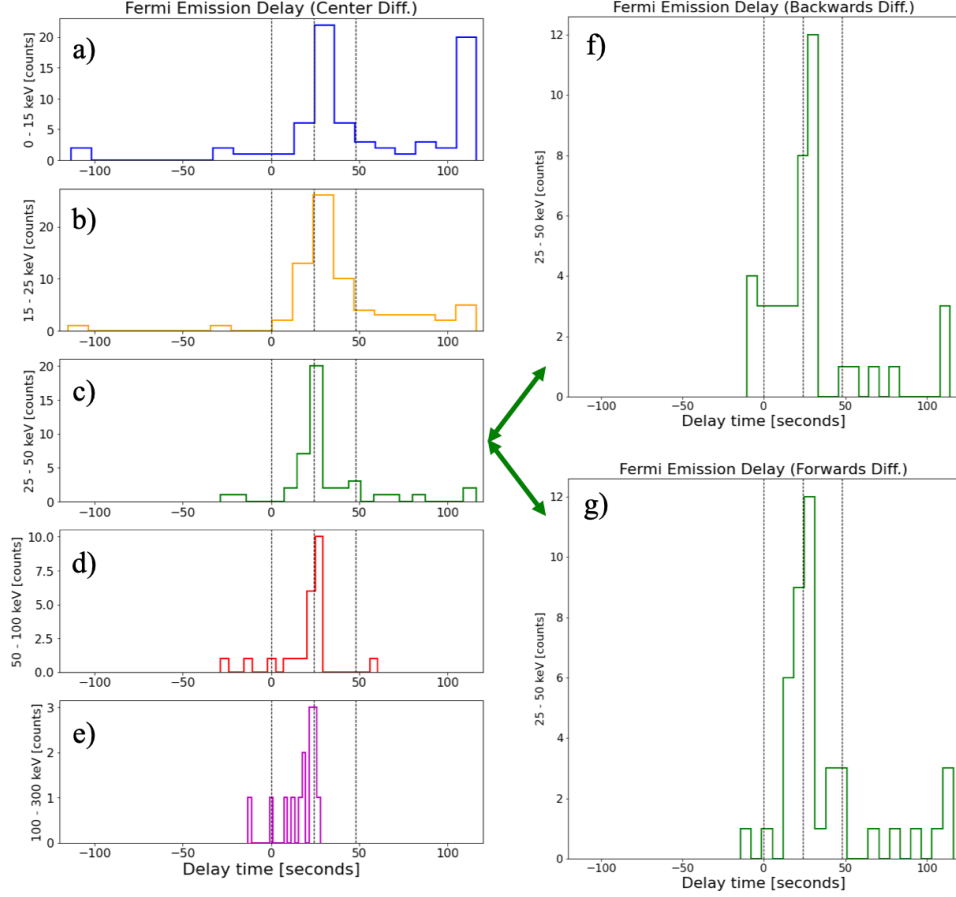


**Figure 8.** Histograms showing the HXR emission delay from reconnection rate maximum (calculated from a central finite difference derivative scheme) for all of the 73 flares with recorded Fermi GBM detections in each energy band: a) 0-15 keV, b) 15-25 keV, c) 25-50 keV, d) 50-100 keV, and e) 100-300 keV. Histograms for the 25-50 keV channel using different finite difference derivative schemes for reconnection rates calculations: f) forward difference, and g) backward difference. Each of the dashed vertical lines show 24 seconds of delay time since from co-temporal emission (delay time of zero seconds). )

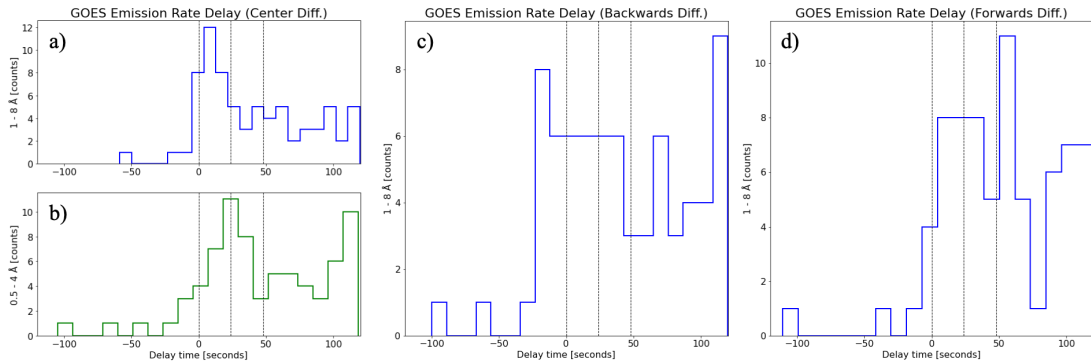


**Figure 9.** Histograms showing the HXR emission delay from reconnection rate maximum (calculated from a central finite difference derivative scheme) for 73 flares with recorded GOES XRS detections in each wavelength band: a) 1-8 Å, and b) 0.5-4 Å. Histograms for the 1-8 Å channel using finite difference derivative schemes for reconnection rate calculations: c) forward difference and d) backward difference.

We find that these fine structures in the flare ribbons provide evidence of the PI instability. In addition we explored the connection of the fine-structure details with the larger scale ribbon sweeping motion and its connection to the QPPs found in our reconnection rate proxies. First, we notice that the AIA 1600 Å lack the spatial resolution to

resolve most if not all of the fine structure that is visible in high resolution SJI observations. Although under-resolved we notice good agreement between the flare ribbon evolution mask derived with AIA and IRIS data. This suggest that the fine-structure contribute to the larger scale bursty evolution observed with AIA 1600 Å data, which we found contributes to the reconnection flux budget in bursty episodes in the reconnection rate.

We discard the possibility that bursts in the reconnection rate are a consequence of a systemic biases in our masking algorithm, since we find reconnection rate QPPs in both positive- and negative-polarity ribbons independently. For example Figure 1, show that although the morphology of the flare ribbon is very different the reconnection flux/rate balance each other through the flare.

Naus et al. (2022) used high resolution IRIS observations to compare evolution of ribbon fronts with HXR emission from Fermi GBM and Reaven Ramaty High Energy Solar Spectroscopic Imager (RHESSI; Lin et al. 2002). They found the ribbon front exhibits highly structured and dynamic changes in their local widths. These intermittent changes in width are compatible with our observations of the ribbon sweeping new reconnected flux and producing bursty reconnection rates. Additionally, the evolution of ribbon front widths is found to be co-spatial and co-temporal with the UV and HXR emission during the late phase of bursty reconnection phase of the flare. This suggests that in the early evolution of the flare, bursty reconnection is required but does not guarantee non-thermal particle acceleration; we find similar decoupling between the reconnection rate and HXR emission in the early phase of the flare, as shown in Figure 4.

Qiu & Cheng (2022), found that the lag in HXR emission to the UV emission from flare ribbons corresponds to the strong-weak magnetic field shear evolution of the flare loops (inferred from flare ribbons). Which is consistent with the 3D MHD simulation by Dahlin et al. (2022), they presented a clear connection between the shear inferred by flare loops and ribbons and the variation of the guide field (magnetic field component perpendicular to the reconnection plane) in the reconnection sheet (where they cannot be measured). Other numerical experiments by Arnold et al. (2021) show that the presence of a strong guide field suppresses the particle acceleration efficiency of plasmoids.

Figure 4 compares evolution of the reconnection rates with the HXR emission from Fermi GBM and with the time derivative of the GOES XRS observations. We find that some large bursts in the reconnection rates are associated with HXR emission in a similar bursty evolution. These results suggest that there is some current sheet dynamics that link these two processes. First we focus on the acceleration in plasmoids (Drake et al. 2006; Guidoni et al. 2016, 2022). This interpretation is compatible with the PI since the current sheet would be filled with plasmoids that can interact at and merge. Single magnetic island accelerators have been found to provide insufficient energy gains to reproduce HXR emission (Drake et al. 2006; Guidoni et al. 2016). Guidoni et al. (2022) analytically showed that transport of electrons between consecutive magnetic islands with similar accelerator efficiencies leads to the non-thermal electron distribution with sufficient energy to produce HXR emission due to electron collisions in the chromosphere. Thus, as these plasmoids are ejected from the current sheet and then reconnect with the flare loops could transfer particle populations to them which could later propagate to the chromosphere.

Additionally, we have found that bursts in the reconnection rates behave like QPPs, and classify periods for 73 flares using the AFINO methodology. Although most reconnection rate time series in our study have a good statistical fit for the QPP model (see Figure 5,  $0.3 < \chi^2 < 1.7$ ; Nita et al. (2014)), we found only 26 of the 73 flares have the QPP model as the preferred model fit ( $\Delta \text{BIC} \leq -10$ ; Burnham & Anderson (2004)). The discrepancy between observed QPPs in the reconnection rates and the AFINO detection can be a consequence of how the BIC statistic penalizes observations with low sample sizes, and many free parameters (see equation 16). This is even more evident when looking at the QPP detections in the Fermi GBM and GOES XRS observations. Figures 6 and 7 show very few detections, and discrepancies between the periods when compared to the reconnection rate periods ( $\geq 5$  minutes). This lower detection of QPPs in the HXR data might be attributed to the existence of lower frequency modes which are excluded from this analysis in order to match the 24 second temporal cadence of the AIA observations. Moreover, as found in Naus et al. (2022) reconnection rate burst are not always accompanied with co-temporal HXR emission burst in the early phase of the flare, which has been associated with the strong-weak magnetic field shear and guide field evolution (Qiu & Cheng 2022; Dahlin et al. 2022) and reduction of the guide field suppression of plasmoid particle acceleration efficiency (Arnold et al. 2021). Therefore, the duration of the HXR QPPs is contained to the impulsive phase of the flare, while the reconnection rate QPPs are usually found throughout the full evolution of the flare, which make difficult the comparison of the QPPs using automatic detection algorithms like AFINO. Another possibility, is that the particle acceleration QPP is driven by different current sheet dynamics like acceleration due to shock within the current sheet.

Other mechanisms to explain QPPs in the reconnection rate include the recent findings of [Thurgood et al. \(2017\)](#) in which magnetic reconnection in a 3D null point can occur periodically and excite MHD waves. A 2D simulation showed that oscillating plasmoids produced by the subsequent merging of two initial plasmoids, can exit oscillations on the current sheet loop tops as they reconnect ([Jelínek et al. 2017](#)). [Takahashi et al. \(2017\)](#) used a 2D simulation of reconnection in a current sheet bellow and eruptive CME and found for large values of the Lundquist number  $S = 5.6 \times 10^3$ , and  $2.8 \times 10^4$  (PI unstable) periodic reconnection produces reconnection jets that excite oscillations at the top and bottom of the current sheet and generate shocks that can accelerate particles with similar QPP periods.

Our study is incapable of distinguishing which of these mechanisms could clearly produce the co-temporal QPPs in the reconnection rates and HXR emission. The spatiotemporal analysis of the flare ribbons suggest that the current sheet undergoes PI and that plasmoids and their dynamics should be related to the generation of the QPPs and bursty signatures presented in this work. Still, we are unable to determine whether the HXR emission is driven by termination shocks produced by the reconnection jets or the merging of magnetic islands populated with accelerated electrons. [Hayes et al. \(2019\)](#) presented on-limb evidence of EUV and SXR QPPs with simultaneous downward motions that impact the flaring loop tops. Therefore co-temporal observation of the on-disk observations of the flare ribbon and off-limb observation of the loop structures during the flare could allow a more complete understanding of the full mechanisms at play for the generation of the QPPs in the HXR emission and reconnection rates. Coordinated observations between SDO (or other ground-based/geosynchronous instrument) and Solar Orbiter ([Müller et al. 2013, 2020](#)) will provide opportunities for this type of study in the windows where the two spacecrafts have a separation angle of  $\approx 90^\circ$ .

Finally, we find that the delay time between the peak reconnection rate burst and the HXR burst peaks is within the range of seconds to minutes, with the modes of the distributions from the Fermi GBM being centered at 24 seconds. Our first intuition was that this delay matches the temporal cadence of the AIA instrument, and therefore could be a consequence of from the numerical differentiation scheme used to approximate the time derivatives of the reconnection flux. We find that this delay is independent of the finite difference scheme, although there is some sensitivity in the GOES XRS HXR proxy. [Miklenic et al. \(2007\)](#); [Veronig & Polanec \(2015\)](#) found similar results when comparing reconnection rates with HXR emission. They interpret the newly brightened  $H_\alpha$ /EUV/UV flaring kernels which are used to track the reconnection flux evolution and HXR emission are being produced by two types of non-thermal electrons. The first type corresponds to a smaller population of non-thermal electrons accelerated within the reconnection site that produces the bright  $H_\alpha$ /EUV/UV kernels. The second larger population of non-thermal particles would accelerate at a different location, possibly at the flare loop tops, providing a delay in the emission burst. To our knowledge there is no observational study, nor simulation that provides evidence to this delay between flare kernels brightening, and the HXR emission and its association to these different non-thermal electron populations.

## 5. CONCLUSIONS

In this study we have analyzed 73 flares included in the RibbonDB database ([Kazachenko et al. 2017](#)), and compared them with Fermi GBM and GOES XRS observations. Our analysis includes the spatio-temporal comparison of flare ribbons observed with AIA 1600 Å and IRIS SJI 1330 Å and 1400 Å (when available), time series of the reconnection fluxes/rates, HXR emission ranging from 0 to 300 keV, and SXR emission/rates in the 1-8 Å and 0.5-4 Å. Our findings are summarized below:

- We find that magnetic reconnection, as described by reconnection rates derived from flare ribbons occurs in bursts. These bursts account for a significant amount of the reconnection budget ranging on average from 0.1 to  $20 \times 10^{20}$  Mx and could be used to compare with models of bursty or oscillatory reconnection. We find 26 cases where these bursty reconnection episodes can be detected as QPPs using the AFINO methodology ([Inglis et al. 2015, 2016](#)). The periods are on the order of minutes ranging from 1 to 11 minute.
- 8 events ranging from C- to X-class flares have corresponding IRIS SJI observations that capture fine structure in the flare ribbons associated with periodic modulations in the ribbon fronts ([Naus et al. 2022](#)), wave-break patterns, and swirls ([Brannon et al. 2015](#); [Wyper & Pontin 2021](#)). These fine-structure patterns have previously been associated with the PI, and the existence of plasmoid structures in the current sheet above the flaring loops.
- Fermi GBM and GOES XRS observations show that HXR bursts are nearly co-temporal, delayed up to a minute from burst in the reconnection rates. The delay time of the Fermi observations is found to have a mode of 24 seconds across five energy bands, suggesting that the particle acceleration of non-thermal particles that interact

with the chromosphere and produce the flaring ribbon kernels and the emission of SXR and HXR might happen at different locations within the current sheet.

- We suggest that nearly co-temporal QPP bursts in the reconnection rates and HXR emission provide evidence of oscillatory process in the reconnection region and plasmoid dynamics (Kliem et al. 2000; Takahashi et al. 2017). This in turn leads to burty particle acceleration via magnetic islands or wave particle interactions (Takahashi et al. 2017; Guidoni et al. 2016; Drake et al. 2006).

We acknowledge support from NASA LWS 80NSSC19K0910, 80NSSC19K0070, NASA ECIP NNH18ZDA001N, NSF CAREER SPVKK1RC2MZ3 (MDK, MFCA). Additionally we would like to thank the Comprehensive Exam Committee for taking their time to read this article, and showing general interest in this project.

## REFERENCES

- Arnold, H., Drake, J., Swisdak, M., et al. 2021, *Physical Review Letters*, 126, 135101, doi: [10.1103/PhysRevLett.126.135101](https://doi.org/10.1103/PhysRevLett.126.135101)
- Atwood, W. B., Abdo, A. A., Ackermann, M., et al. 2009, *Astrophysical Journal*, 697, 1071, doi: [10.1088/0004-637X/697/2/1071](https://doi.org/10.1088/0004-637X/697/2/1071)
- Bárta, M., Karlický, M., & Žemlička, R. 2008, *Solar Physics*, 253, 173, doi: [10.1007/s11207-008-9217-5](https://doi.org/10.1007/s11207-008-9217-5)
- Benz, A. O. 2017, *Living Reviews in Solar Physics*, 14, doi: [10.1007/s41116-016-0004-3](https://doi.org/10.1007/s41116-016-0004-3)
- Bobra, M. G., Xudong, S., & Turmon, M. J. 2021, doi: [10.5281/ZENODO.5131292](https://doi.org/10.5281/ZENODO.5131292)
- Bornmann, P. L., Speich, D., Hirman, J., et al. 1996, in *GOES-8 and Beyond*, ed. E. R. Washwell, Vol. 2812 (SPIE), 291–298, doi: [10.1117/12.254076](https://doi.org/10.1117/12.254076)
- Brannon, S. R., Longcope, D. W., & Qiu, J. 2015, *The Astrophysical Journal*, 810, 4, doi: [10.1088/0004-637X/810/1/4](https://doi.org/10.1088/0004-637X/810/1/4)
- Broomhall, A. M., Davenport, J. R., Hayes, L. A., et al. 2019, *arXiv*, 244, 44, doi: [10.3847/1538-4365/ab40b3](https://doi.org/10.3847/1538-4365/ab40b3)
- Brown, J. C. 1971, *Solar Physics*, 18, 489, doi: [10.1007/BF00149070](https://doi.org/10.1007/BF00149070)
- Burnham, K. P., & Anderson, D. R. 2004, *Sociological Methods & Research*, 33, 261, doi: [10.1177/0049124104268644](https://doi.org/10.1177/0049124104268644)
- Carmichael, H. 1964, in *The Physics of Solar Flares*, 451–456. <https://ui.adsabs.harvard.edu/abs/1964NASSP..50..451C/abstract>
- Chamberlin, P. C., Woods, T. N., Eparvier, F. G., & Jones, A. R. 2009, in *Solar Physics and Space Weather Instrumentation III*, ed. S. Fineschi & J. A. Fennelly, Vol. 7438 (SPIE), 743802, doi: [10.1117/12.826807](https://doi.org/10.1117/12.826807)
- Dahlin, J. T., Antiochos, S. K., Qiu, J., & DeVore, C. R. 2022, *The Astrophysical Journal*, 932, 94, doi: [10.3847/1538-4357/ac6e3d](https://doi.org/10.3847/1538-4357/ac6e3d)
- De Pontieu, B., Polito, V., Hansteen, V., et al. 2021, *Solar Physics*, 296, 84, doi: [10.1007/s11207-021-01826-0](https://doi.org/10.1007/s11207-021-01826-0)
- De Pontieu, B., Title, A. M., Lemen, J. R., et al. 2014, *Solar Physics*, 289, 2733, doi: [10.1007/s11207-014-0485-y](https://doi.org/10.1007/s11207-014-0485-y)
- Drake, J. F., Swisdak, M., Che, H., & Shay, M. A. 2006, *Nature*, 443, 553, doi: [10.1038/nature05116](https://doi.org/10.1038/nature05116)
- Forbes, T., & Lin, J. 2000, *Journal of Atmospheric and Solar-Terrestrial Physics*, 62, 1499, doi: [10.1016/S1364-6826\(00\)00083-3](https://doi.org/10.1016/S1364-6826(00)00083-3)
- Furth, H. P., Killeen, J., & Rosenbluth, M. N. 1963, *Physics of Fluids*, 6, 459, doi: [10.1063/1.1706761](https://doi.org/10.1063/1.1706761)
- Guidoni, S. E., DeVore, C. R., Karpen, J. T., & Lynch, B. J. 2016, *The Astrophysical Journal*, 820, 60, doi: [10.3847/0004-637x/820/1/60](https://doi.org/10.3847/0004-637x/820/1/60)
- Guidoni, S. E., Karpen, J. T., & DeVore, C. R. 2022, *The Astrophysical Journal*, 925, 191, doi: [10.3847/1538-4357/ac39a5](https://doi.org/10.3847/1538-4357/ac39a5)
- Harris, C. R., Millman, K. J., van der Walt, S. J., et al. 2020, *Nature*, 585, 357, doi: [10.1038/s41586-020-2649-2](https://doi.org/10.1038/s41586-020-2649-2)
- Hayes, L. A., Gallagher, P. T., Dennis, B. R., et al. 2019, *arXiv*, 875, 33, doi: [10.3847/1538-4357/ab0ca3](https://doi.org/10.3847/1538-4357/ab0ca3)
- Hirayama, T. 1974, *Solar Physics*, 34, 323, doi: [10.1007/BF00153671](https://doi.org/10.1007/BF00153671)
- Hoeksema, J. T., Liu, Y., Hayashi, K., et al. 2014, *Solar Physics*, 289, 3483, doi: [10.1007/s11207-014-0516-8](https://doi.org/10.1007/s11207-014-0516-8)
- Hudson, H. S. 2011, *Space Science Reviews*, 158, 5, doi: [10.1007/s11214-010-9721-4](https://doi.org/10.1007/s11214-010-9721-4)
- Inglis, A. R., Ireland, J., Dennis, B. R., Hayes, L., & Gallagher, P. 2016, *The Astrophysical Journal*, 833, 284, doi: [10.3847/1538-4357/833/2/284](https://doi.org/10.3847/1538-4357/833/2/284)
- Inglis, A. R., Ireland, J., & Dominique, M. 2015, *Astrophysical Journal*, 798, doi: [10.1088/0004-637X/798/2/108](https://doi.org/10.1088/0004-637X/798/2/108)
- Jelínek, P., Karlický, M., Van Doorselaere, T., & Bárta, M. 2017, *The Astrophysical Journal*, 847, 98, doi: [10.3847/1538-4357/aa88a6](https://doi.org/10.3847/1538-4357/aa88a6)
- Kazachenko, M. D., Lynch, B. J., Welsch, B. T., & Sun, X. 2017, *The Astrophysical Journal*, 845, 49, doi: [10.3847/1538-4357/aa7ed6](https://doi.org/10.3847/1538-4357/aa7ed6)

- Kliem, B., Karlický, M., & Benz, A. O. 2000, *Astron. Astrophys.*, 360, 715. <https://ui.adsabs.harvard.edu/abs/2000A%26A...360..715K/abstract>
- Kopp, R., & Pneuman, G. 1976, *Solar Physics*, 50, doi: [10.1007/BF00206193](https://doi.org/10.1007/BF00206193)
- Lemen, J. R., Title, A. M., Akin, D. J., et al. 2012, *Solar Physics*, 275, 17, doi: [10.1007/s11207-011-9776-8](https://doi.org/10.1007/s11207-011-9776-8)
- Lin, R., Dennis, B., Hurford, G., et al. 2002, *Solar Physics*, 210, 3, doi: [10.1023/A:1022428818870](https://doi.org/10.1023/A:1022428818870)
- Loureiro, N. F., Schekochihin, A. A., College, K., & Cowley, S. C. 2007, *Physics of Plasmas*, 14, doi: [10.1063/1.2783986](https://doi.org/10.1063/1.2783986)
- Lynch, B. J., Edmondson, J. K., Kazachenko, M. D., & Guidoni, S. E. 2016, *ApJ*, 826, 43, doi: [10.3847/0004-637X/826/1/43](https://doi.org/10.3847/0004-637X/826/1/43)
- Machol, J. L., Eparvier, F. G., Viereck, R. A., et al. 2019, in *The GOES-R Series: A New Generation of Geostationary Environmental Satellites* (Elsevier), 233–242, doi: [10.1016/B978-0-12-814327-8.00019-6](https://doi.org/10.1016/B978-0-12-814327-8.00019-6)
- McLaughlin, J. A., Nakariakov, V. M., Dominique, M., Jelínek, P., & Takasao, S. 2018, *Space Science Reviews*, 214, 45, doi: [10.1007/s11214-018-0478-5](https://doi.org/10.1007/s11214-018-0478-5)
- Meegan, C., Lichti, G., Bhat, P. N., et al. 2009, *Astrophysical Journal*, 702, 791, doi: [10.1088/0004-637X/702/1/791](https://doi.org/10.1088/0004-637X/702/1/791)
- Miklenic, C. H., Veronig, A. M., Vršnak, B., & Hanslmeier, A. 2007, *Astronomy and Astrophysics*, 461, 697, doi: [10.1051/0004-6361:20065751](https://doi.org/10.1051/0004-6361:20065751)
- Müller, D., Marsden, R. G., St. Cyr, O. C., & Gilbert, H. R. 2013, *Solar Physics*, 285, 25, doi: [10.1007/s11207-012-0085-7](https://doi.org/10.1007/s11207-012-0085-7)
- Müller, D., St. Cyr, O. C., Zouganelis, I., et al. 2020, *Astronomy & Astrophysics*, 642, A1, doi: [10.1051/0004-6361/202038467](https://doi.org/10.1051/0004-6361/202038467)
- Mumford, S., Freij, N., Christe, S., et al. 2020, *Journal of Open Source Software*, 5, 1832, doi: [10.21105/joss.01832](https://doi.org/10.21105/joss.01832)
- Mumford, S. J., Freij, N., Stansby, D., et al. 2022, doi: [10.5281/ZENODO.7074315](https://doi.org/10.5281/ZENODO.7074315)
- Nakariakov, V. M., & Melnikov, V. F. 2009, *Space Science Reviews*, 149, 119, doi: [10.1007/s11214-009-9536-3](https://doi.org/10.1007/s11214-009-9536-3)
- Naus, S. J., Qiu, J., DeVore, C. R., et al. 2022, *The Astrophysical Journal*, 926, 218, doi: [10.3847/1538-4357/ac4028](https://doi.org/10.3847/1538-4357/ac4028)
- Neupert, W. M. 1968, *The Astrophysical Journal*, 153, L59, doi: [10.1086/180220](https://doi.org/10.1086/180220)
- Nita, G. M., Fleishman, G. D., Gary, D. E., Marin, W., & Boone, K. 2014, *The Astrophysical Journal*, 789, 152, doi: [10.1088/0004-637X/789/2/152](https://doi.org/10.1088/0004-637X/789/2/152)
- Parker, E. N. 1957, *Journal of Geophysical Research*, 62, 509, doi: [10.1029/JZ062i004p00509](https://doi.org/10.1029/JZ062i004p00509)
- . 1963, *The Astrophysical Journal Supplement Series*, 8, 177, doi: [10.1086/190087](https://doi.org/10.1086/190087)
- Parker, J., & Longcope, D. 2017, *The Astrophysical Journal*, 847, 30, doi: [10.3847/1538-4357/aa8908](https://doi.org/10.3847/1538-4357/aa8908)
- Pesnell, W. D., Thompson, B. J., & Chamberlin, P. C. 2012, *Solar Physics*, 275, 3, doi: [10.1007/s11207-011-9841-3](https://doi.org/10.1007/s11207-011-9841-3)
- Petschek, H. E. 1964, *NASA Special Publication*, 50, 425
- Pontin, D. I., & Priest, E. R. 2022, *Living Reviews in Solar Physics*, 19, 1, doi: [10.1007/s41116-022-00032-9](https://doi.org/10.1007/s41116-022-00032-9)
- Priest, E., & Forbes, T. 2002, *The Astronomy and Astrophysics Review*, 10, 313, doi: [10.1007/s001590100013](https://doi.org/10.1007/s001590100013)
- Qiu, J., & Cheng, J. 2022, *Solar Physics*, 297, 80, doi: [10.1007/s11207-022-02003-7](https://doi.org/10.1007/s11207-022-02003-7)
- Shibata, K., & Magara, T. 2011, *Living Reviews in Solar Physics*, 8, doi: [10.12942/lrsp-2011-6](https://doi.org/10.12942/lrsp-2011-6)
- Shibata, K., & Tanuma, S. 2001, *Earth, Planets and Space*, 53, 473, doi: [10.1186/BF03353258](https://doi.org/10.1186/BF03353258)
- Sturrock, P. A. 1966, *Nature*, 211, 695, doi: [10.1038/211695a0](https://doi.org/10.1038/211695a0)
- Sun, X. 2013. <http://arxiv.org/abs/1309.2392>
- Sweet, P. A. 1958a, in *Electromagnetic Phenomena in Cosmical Physics*, ed. B. Lehnert (Cambridge, U.K.: Cambridge University Press), 123–134
- . 1958b, *Nuovo Cimento*, 8, 188
- Takahashi, T., Qiu, J., & Shibata, K. 2017, *The Astrophysical Journal*, 848, 102, doi: [10.3847/1538-4357/aa8f97](https://doi.org/10.3847/1538-4357/aa8f97)
- The Astropy Collaboration, Price-Whelan, A. M., Lim, P. L., et al. 2022, *The Astrophysical Journal*, 935, 167, doi: [10.3847/1538-4357/ac7c74](https://doi.org/10.3847/1538-4357/ac7c74)
- Thurgood, J. O., Pontin, D. I., & McLaughlin, J. A. 2017, *The Astrophysical Journal*, 844, 2, doi: [10.3847/1538-4357/aa79fa](https://doi.org/10.3847/1538-4357/aa79fa)
- Uzdensky, D. A., Loureiro, N. F., & Schekochihin, A. A. 2010, *Physical Review Letters*, 105, doi: [10.1103/PhysRevLett.105.235002](https://doi.org/10.1103/PhysRevLett.105.235002)
- Van Doorselaere, T., Kupriyanova, E. G., & Yuan, D. 2016, *Solar Physics*, 291, 3143, doi: [10.1007/s11207-016-0977-z](https://doi.org/10.1007/s11207-016-0977-z)
- Vaughan, S. 2005, *Astronomy & Astrophysics*, 431, 391, doi: [10.1051/0004-6361:20041453](https://doi.org/10.1051/0004-6361:20041453)
- Veronig, A. M., & Polanec, W. 2015, *Solar Physics*, 290, 2923, doi: [10.1007/s11207-015-0789-6](https://doi.org/10.1007/s11207-015-0789-6)
- Virtanen, P., Gommers, R., Oliphant, T. E., et al. 2020, *Nature Methods*, 17, 261, doi: [10.1038/s41592-019-0686-2](https://doi.org/10.1038/s41592-019-0686-2)
- Wyper, P. F., & Pontin, D. I. 2021, *The Astrophysical Journal*, 920, 102, doi: [10.3847/1538-4357/ac1943](https://doi.org/10.3847/1538-4357/ac1943)